Comparing inclination-dependent analyses of kilonova transients

J. Heinzel,[1,2]★ M. W. Coughlin [ORCID],[2]★ T. Dietrich,[3] M. Bulla [ORCID],[4] S. Antier [ORCID],[5] N. Christensen,[1,6] D. A. Coulter,[7] R. J. Foley,[7] L. Issa[4,8] and N. Khetan[9]

[1]*Carleton College, Northfield, MN 55057, USA*
[2]*School of Physics and Astronomy, University of Minnesota, Minneapolis, MN 55455, USA*
[3]*Institute of Physics and Astronomy, University of Potsdam, D-14476 Potsdam, Germany*
[4]*Nordita, KTH Royal Institute of Technology and Stockholm University, Roslagstullsbacken 23, SE-106 91 Stockholm, Sweden*
[5]*APC, UMR 7164, 10 rue Alice Domon et Léonie Duquet, F-75205 Paris, France*
[6]*Artemis, Université Côte d'Azur, Observatoire Côte d'Azur, CNRS, CS 34229, F-06304 Nice Cedex 4, France*
[7]*Department of Astronomy and Astrophysics, University of California, Santa Cruz, CA 95064, USA*
[8]*Université Paris-Saclay, ENS Paris-Saclay, Département de Physique, F-91190 Gif-sur-Yvette, France*
[9]*Gran Sasso Science Institute (GSSI), I-67100 L'Aquila, Italy*

ABSTRACT

The detection of the optical transient AT2017gfo proved that binary neutron star mergers are progenitors of kilonovae (KNe). Using a combination of numerical-relativity and radiative-transfer simulations, the community has developed sophisticated models for these transients for a wide portion of the expected parameter space. Using these simulations and surrogate models made from them, it has been possible to perform Bayesian inference of the observed signals to infer properties of the ejected matter. It has been pointed out that combining inclination constraints derived from the KN with gravitational-wave measurements increases the accuracy with which binary parameters can be estimated, in particular breaking the distance-inclination degeneracy from gravitational wave inference. To avoid bias from the unknown ejecta geometry, constraints on the inclination angle for AT2017gfo should be insensitive to the employed models. In this work, we compare different assumptions about the ejecta and radiative reprocesses used by the community and we investigate their impact on the parameter inference. While most inferred parameters agree, we find disagreement between posteriors for the inclination angle for different geometries that have been used in the current literature. According to our study, the inclusion of reprocessing of the photons between different ejecta types improves the modeling fits to AT2017gfo and, in some cases, affects the inferred constraints. Our study motivates the inclusion of large $\sim$ 1-mag uncertainties in the KN models employed for Bayesian analysis to capture yet unknown systematics, especially when inferring inclination angles, although smaller uncertainties seem appropriate to capture model systematics for other intrinsic parameters. We can use this method to impose soft constraints on the ejecta geometry of the KN AT2017gfo.

Key words: gravitational waves – neutron star mergers – radiative transfer – methods: numerical – stars: neutron.

1 INTRODUCTION

Multimessenger astronomy is driven by the idea that the observation of a single system with multiple messengers yields a more complete picture of the astrophysical processes than individual observational channels could provide. Indeed, the first combined detection of gravitational waves (GWs), GW170817 (Abbott et al. 2017), and electromagnetic (EM) signals, AT2017gfo and GRB170817A (Alexander et al. 2017; Chornock et al. 2017; Cowperthwaite et al. 2017; Drout et al. 2017; Evans et al. 2017; Haggard et al. 2017; Hallinan et al. 2017; Kasliwal et al. 2017; Kilpatrick et al. 2017; Margutti et al. 2017; McCully et al. 2017; Nicholl et al. 2017; Pian et al. 2017; Shappee et al. 2017; Smartt et al. 2017; Troja et al. 2017; Utsumi et al. 2017), from the merger of two neutron stars has been a proof of the concept that a multi-messenger approach can be successful

to constrain the supranuclear equation of state (EOS) of matter (e.g. Bauswein et al. 2017; Annala et al. 2018; Coughlin et al. 2018, 2019; Most et al. 2018; Radice et al. 2018a; Capano et al. 2019; Radice & Dai 2019; Dietrich et al. 2020) or to measure the expansion rate of the Universe (e.g. Abbott et al. 2017; Hotokezaka et al. 2019; Coughlin et al. 2020a,b; Dietrich et al. 2020). It has, however, been pointed out that even small systematic uncertainties can bias the Hubble constant constraint significantly (Chen 2020).

Kilonovae (KNe; Lattimer & Schramm 1974; Li & Paczynski 1998; Metzger et al. 2010; Roberts et al. 2011; Kasen et al. 2017) transients in the infrared, optical, and ultraviolet bands are triggered by the radioactive decay of r-process elements produced in neutron-rich ejecta released during and after the merger process. In general, not all binary systems are expected to create KNe, e.g. binary neutron star (BNS) systems with too high total masses (Bauswein, Baumgarte & Janka 2013; Agathos et al. 2019; Köppel, Bovard & Rezzolla 2019; Bauswein et al. 2020) or black hole-neutron star (BHNS) systems with sufficiently large mass ratio, aligned black

★ E-mail: heinzelj@carleton.edu (JH); cough052@umn.edu (MWC)

hole spins, or compact neutron stars (Pannarale, Tonita & Rezzolla 2011; Foucart 2012; Kawaguchi et al. 2016a; Foucart, Hinderer & Nissanke 2018; Krüger & Foucart 2020).

In the case of AT2017gfo, the KN signal started out as very blue, before reddening on a time-scale of a few hours to days. While there are still a few possible scenarios to explain the initial, early emission signature (Arcavi 2018), the red component is likely to be characteristic for almost all KNe originating from the merger of two neutron stars as well as from a BHNS merger (for a review, see Metzger 2020 and references therein). Continuous efforts within the theoretical astrophysics community over the last years allowed the observed bolometric and photometric data to be connected with theoretical KN models based on full radiative-transfer simulations (e.g. Tanaka & Hotokezaka 2013; Kawaguchi et al. 2016b; Kasen et al. 2017; Burns et al. 2018; Bulla 2019) or analytical/semi-analytical KN models (e.g. Dietrich & Ujevic 2017; Perego, Radice & Bernuzzi 2017; Kawaguchi, Shibata & Tanaka 2018).

Although KNe are likely observable from all directions and not beamed as short gamma-ray bursts, numerical relativity simulations (e.g. Hotokezaka et al. 2013; Dietrich & Ujevic 2017; Radice et al. 2018b) indicate that the ejected matter in a neutron-star merger is not perfectly spherical. Thus, not only does the photon emission show a clear angular dependence, but the entire ejecta geometry can as well. Broadly speaking, there are at least two geometric sections of the KN: First, the material ejected around the moment of merger via torque and shocks, called the *dynamical ejecta*, with light r-process material primarily distributed in the polar regions and heavier tidal r-process material concentrated towards the equatorial plane, (e.g. Wanajo et al. 2014; Kawaguchi et al. 2016a; Dietrich & Ujevic 2017). The second section is ejected after the merger by winds produced from the remnant system due to neutrino emission, magnetic fields, or secular effects that drive further ejection (e.g. Dessart et al. 2009; Perego et al. 2014; Fernández et al. 2015; Kasen, Fernandez & Metzger 2015; Kiuchi et al. 2015; Martin et al. 2015; Foucart et al. 2016; Siegel & Metzger 2017; Radice et al. 2018b). This component is called the *disc wind*, and is often approximated as being free of heavier r-process material.

KNe are often simulated by radiative transfer algorithms, which simulate emission and propagation of radiation in r-process material. Since the distribution of radioactive material is directly related to the distribution of mass, assumptions must be made about the underlying geometry and behaviour of the ejected material. These geometries are a critical assumption, as they directly lead to inference on parameters such as the inclination or mass of the ejected material, which then are tied back to progenitor parameters.

In this paper, we will use several different KN geometries and the radiative transfer code POSSIS developed by Bulla (2019) to understand how inclination constraints on GW170817/AT2017gfo depend on the underlying geometry assumed, extending the work of Dhawan et al. (2019) and complementary to the work of Kóbori, Bagoly & Balázs (2020). In Section 2, we discuss the creation of surrogate models based on KN geometries inspired by Kasen et al. (2017), Wollaeger et al. (2018), and Bulla (2019). These surrogate models are direct extensions of Coughlin et al. (2018) and provide a phenomenological description of inclination effects. In Section 3, we compare the surrogate models against each other, in particular investigating possible systematic biases and uncertainties and explore how each of the surrogate models derived in Section 2 provide constraints on the inclination angle of GW170817/AT2017gfo, the total ejected mass, and the dynamical-to-disc wind mass ratio. We conclude in Section 4 and outline avenues for future work.

2 KN MODELS AND SURROGATE CONSTRUCTION

In the following, we explore three different models that simulate multiple viewing-angle-dependent components. It has become common to simulate ejecta separately, then add the light curves in flux space after simulation (e.g. Kasen et al. 2017; Villar et al. 2017; Coughlin et al. 2018), which neglects any sort of *reprocessing* between multiple components, when radiation from one component is absorbed and re-radiated at a different wavelength by the other component. We also examine how accounting for this reprocessing can change the light-curve fitting to AT2017gfo and the inferred posteriors on the system parameters (cf. Kawaguchi et al. 2018).

All models that we investigate are axially symmetric, following the precedent of e.g. Kasen et al. (2017), Wollaeger et al. (2018), Bulla (2019), Kawaguchi, Shibata & Tanaka (2020), and Korobkin et al. (2020). Thus, our radiative transfer simulations give us inclination-dependent (but azimuthal independent) light curves, where we compute light curves for 11 different inclination angles $\theta_{\rm obs}$ using a uniform spacing in $\cos\theta_{\rm obs}$.

2.1 POSSIS

Bulla (2019) developed a radiative transfer code POSSIS, in which initially a spherical KN geometry had been employed with a lanthanide-rich component near the equatorial region and a lanthanide-free component towards the poles; see the left-hand panel of Fig. 1, labelled SSCr. Bound–bound opacities are treated as either 'rich' (electron fraction $Y_{\rm e} \leq 0.25$) or 'free' ($Y_{\rm e} > 0.25$) in POSSIS, with their wavelength- and time-dependence chosen to mimic realistic opacities based on atomic calculations from Tanaka et al. (2018).

POSSIS creates photon packets based on the distribution of radioactive material and emits them isotropically. The frequencies of the photon packets produced are sampled from the thermal emissivity at the precise location, and photon packet energy is determined from nuclear heating rates in Korobkin et al. (2012).

POSSIS propagates the photon packets through the ejecta (assumed to expand homologously) until they interact with matter. It then probabilistically decides whether this interaction is governed by electron scattering, or by a bound–bound, bound–free, or free–free opacity. In electron scattering, the frequency is unchanged (in the interaction frame) and the new direction is sampled from a scattering probability distribution (see equation 12 of Bulla, Sim & Kromer 2015). If a bound–bound transition occurs, Bulla (2019) uses the two-level atom approach (TLA) of Kasen, Thomas & Nugent (2006), where the photon packet is re-emitted 10 per cent of the time with the same frequency while 90 per cent of the time with a new frequency sampled from the location's thermal emissivity. The TLA approach is meant to model the complex behaviour of re-emitting a photon through many different possible line transitions (for more detailed investigation on the assumptions inherent to the TLA approach, see equation 7 and section 3.6 of Kasen et al. 2006). Bound–free and free–free processes are subdominant at the relevant wavelengths for KNe (Tanaka et al. 2018) and are thus typically negligible.

We used an improved version of POSSIS, which instead of taking a fixed value for the thermalization efficiency ($\epsilon {\rm th} = 0.5$), now takes its temporal evolution into account, with values approximated by Barnes et al. (2016). Furthermore, temperature is no longer a free parameter, and is estimated self-consistently from the mean intensity of the radiation (Carracedo et al. 2020; Coughlin et al. 2020b)
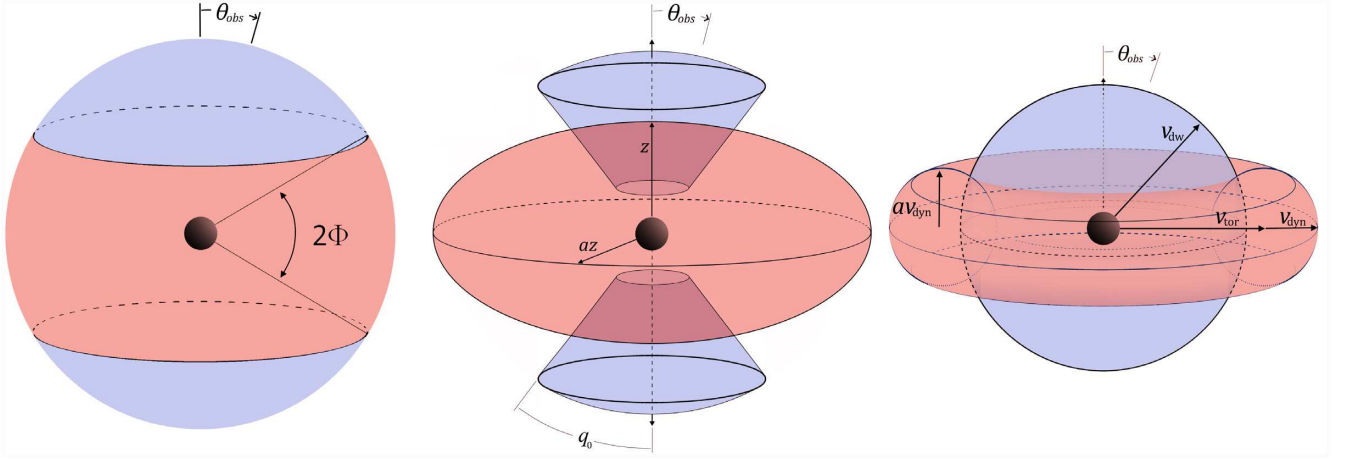
Figure 1. Depictions of the ejecta geometries of the SSCr model in the left-hand panel, the ElDC model in the middle panel, and the TorS model in the right-hand panel. Blue colours refer to lanthanide-free regions and red refers to lanthanide-rich regions. On the left-hand panel, Coughlin et al. (2020b) defined their half-opening angle for the lanthanide-rich region Φ to be analogous to $90° - q_0$, where q_0 is the half-opening angle for the lanthanide-free conal region as defined by Kasen et al. (2017); we use the same definitions for the SSCr model. In the middle panel, we show Kasen et al. (2017)'s ejecta geometries; Kasen et al. (2017) simulated aspect ratios a of $a = 2$ or $a = 4$, with only the polar dynamical ejecta, and the half-opening angle of the polar dynamical ejecta fixed to be $q_0 = 45°$. We show the ElDC geometry for these parameters. On the right-hand panel, Wollaeger et al. (2018) simulated the tidal dynamical ejecta according to direct numerical relativity simulations; in our simulations (the TorS model), we adopted an approximation of their technique.

2.2 Spherical segment-spherical cap (SSCr) geometry

Due to the relatively fast analysis speeds – a typical simulation takes a few hours to a day on a single core – Coughlin et al. (2020b) were able to use POSSIS to simulate their KN model over a full grid of two parameter values for their geometry (Fig. 1, left-hand panel) – half-opening angle Φ, and total ejecta mass M_{ej}. We use the 50 simulations from Coughlin et al. (2020b), and call it the SSCr reprocessing geometry, based on its qualitative shape (see Fig. 1). Since reprocessing, i.e. when radiation from one ejecta component is absorbed by the other and re-radiated at a different wavelength, between the two components was naturally incorporated in the simulations from Coughlin et al. (2020b), we will refer to this geometry as SSCr to be consistent with the other KN models described below.

The density profile used by the SSCr model is spherically symmetric and follows an inverse power-law profile given by

$$\rho(r) \propto r^{-\beta}, \qquad (1)$$

where $\beta = 3$ is taken to match hydrodynamical simulations (Hotokezaka et al. 2013; Tanaka & Hotokezaka 2013). Explicitly then, there is no difference between the treatment of density in the lanthanide-rich component versus the lanthanide-free component (Bulla 2019).

2.3 Ellipsoidal-double cone (ElDC) geometry

Kasen et al. (2017) explored non-spherical geometries by using a two-dimensional axially symmetric geometry, with separate components for the polar dynamical ejecta and the disc wind ejecta. For the polar ejecta, they used an ad hoc, broken power-law density profile describing the distribution of the ejected material (with mass $M_{ej, 1}$) over varying radii and velocities, declining gradually in the interior but dropping steeply in the outer layers:

$$\rho_{pol}(r, \theta_{obs}, t) = \rho(r, t) \left[1 + \left(\frac{f(\theta_{obs})}{f_0} \right)^{10} \right]^{-1}, \qquad (2)$$

where $\rho_{pol}(r, \theta_{obs}, t)$ is the density profile we used for the polar ejecta, $\rho(r, t)$ is the normalized spherical density profile, shown in equation (4) of Kasen et al. (2017), $f(\theta) = 1 - \cos(\theta)$, and $f_0 = 1 - \cos(q_0)$. The idea is that the formula concentrates the ejecta in the polar cone with half-opening angle q_0.

For the disc wind, Kasen et al. (2017) used an oblate ellipsoid density profile, which stretched the axes in the equatorial plane by the factor a,

$$\rho_{dw}(x, y, z, t) = \rho(r_{ell}, t); \qquad r_{ell} = \sqrt{z^2 + (x^2 + y^2)/a^2}, \quad (3)$$

with $\rho(r, t)$ again as the normalized spherical density profile in equation (4) in Kasen et al. (2017), x, y, z, t are the ordinary coordinates in Cartesian spacetime, and r_{ell} defines the ellipsoidal isodensity surfaces (as in equations 25–26 of Bulla et al. 2015). We then re-normalize the total mass in the disc wind $M_{ej, 2}$, as stretching the axes in this way without changing the total mass. The disc wind ellipsoid model parameters simulated in that work were fixed to an ejecta mass $M_{ej, 2} = 0.04\,M_\odot$, an ejecta velocity $v_{ej} = 0.1c$, and a lanthanide fraction $X_{lan} = 10^{-2}$. The axial ratio and opening angle assumed in their work were $a = 4$ and $q_0 = 45°$, respectively.

In our analysis, we extended these two geometry grids for the disc wind and polar dynamical ejecta formulations, and simulated a grid of geometries with the four parameters $M_{ej, 1}$, $M_{ej, 2}$, q_0, and a, outlined in Table 1. We refer to this model as the EIDC (ElDC) model. We *first* simulate the disc wind and dynamical geometries separately, i.e. we have a 'dynamical' simulation set and a 'disc wind' simulation set. As done in e.g. Kasen et al. (2017), Villar et al. (2017), and Coughlin et al. (2018), we add the light curves together, first converting to flux space, and then back into magnitudes.

Given the speed of POSSIS, it is possible to combine the geometries to investigate 'reprocessing' effects, when radiation escaping from one ejecta component is absorbed by the other and re-radiated at the same or at a different frequency (see Section 2.1). To do so, we combined these two geometries together into a single geometry by superimposing each disc wind with each dynamical geometry. Rather than superimpose the ejecta directly and mix the lanthanide fractions, we take a different approach. Because of how POSSIS

Table 1. Summary of the parameters in the ElDC geometry simulated in POSSIS.

Ejecta type	Parameter	Parameter values
Dynamical	$M_{ej,\,1}$	[0.001, 0.01, 0.025, 0.04, 0.055, 0.07, 0.085, 0.1] $M_\odot$
Dynamical	q_0	[15°, 30°, 45°, 60°, 75°]
Disc wind	$M_{ej,\,2}$	[0.001, 0.01, 0.025, 0.04, 0.055, 0.07, 0.085, 0.1] $M_\odot$
Disc wind	a	[1, 2, 4, 6, 8]

Notes. $M_{ej,\,1}$ refers to the total mass in the lanthanide-free region, q refers to the half-opening angle of the lanthanide-free region, $M_{ej,\,2}$ refers to the total mass in the lanthanide-rich region, and a refers to the axial ratio between the equatorial radius and the height of the lanthanide-rich disc wind. See the middle panel of Fig. 1 for a depiction of q_0 and a in the ElDC model.

treats lanthanide opacities, we needed to ensure directly that the masses allocated to each component were what we desired. For each cell, the lanthanide fraction is taken to be lanthanide-rich if the density contribution from the dynamical component is higher than the contribution from the disc wind, and lanthanide-free if the opposite is true. The total mass of each ejecta is then rescaled to match the desired mass in each ejecta. Since this may mean some cells identified as lanthanide-free should become lanthanide-rich (or vice-versa), the above process is done iteratively until a stable point is found, that is, when there are no more cells that switch from lanthanide-free to lanthanide-rich. If the process gets stuck in a meta-stable loop, the process is terminated (usually only a few cells are affected in this case). We refer to the simulation set with reprocessing as the ElDC reprocessing (ElDCr) model.

It is important to note that in the typical method, where ejecta geometries are simulated separately, only a grid of $8 \times 5 + 8 \times 5 = 80$ simulations (see Table 1; 8 $M_{ej,\,1}$ parameter values, 5 q_0 parameter values combines to 40 dynamical simulations, and 8 $M_{ej,\,2}$ parameter values, 5 a parameter values combines to 40 disc wind simulations, so 80 total) were needed to cover necessary parameter space. When multiple geometries are reprocessed, $8 \times 5 \times 8 \times 5 = 1600$ simulations were necessary. So this is a case where computational efficiency is sacrificed for modeling accuracy.

2.4 Toroidal-spherical (TorS) geometry

We also employ POSSIS to simulate geometries similar to those presented in Wollaeger et al. (2018). To match Wollaeger et al. (2018), we define our geometry in terms of velocity space, but since the ejecta is assumed to expand homologously, the transformation from velocity space to ordinary space is simply $r = vt$. In other words, defining the ejecta geometry in velocity space is equivalent to defining it in ordinary space, and the geometry in velocity space is identical to the geometry in ordinary position space. Wollaeger et al. (2018) also used a two-component model, simulating only *tidal* dynamical ejecta directly, using long-term numerical relativity (NR) simulations directly from Rosswog et al. (2014), treated as lanthanide-rich in composition. For the second component, they simulated a spherical disc wind treated as lanthanide-poor (so lanthanide-free in our simulations), with the density profile

$$\rho_{dw}(v) = \rho_0 \left(1 - \frac{v^2}{v_{dw}^2}\right)^3, \tag{4}$$

where ρ_0 is a coefficient proportional to the total ejecta mass, and v is the independent variable velocity analogous to r in Sections 2.2
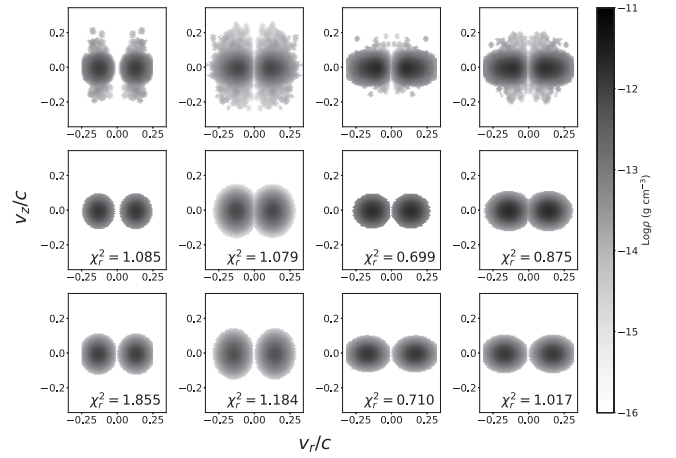
Figure 2. A comparison between the axially averaged Rosswog et al. (2014) models used in Wollaeger et al. (2018) (top panels), the χ^2 minimization of equation (5) with respect to all five parameters: ρ_0, v_{tor}, a, σ, and v_{dyn} (middle panels), and the χ^2 minimization of equation (5) with $v_{tor} = 0.059c + v_{dyn}$ and $\sigma = v_{dyn}/3.5$ fixed (bottom panels). From the left- to right-hand side are the simulations A, B, C, and D from Rosswog et al. (2014).

and 2.3. Wollaeger et al. (2018) fixed $v_{dw} = 0.15c$, whereas in the following, we treat v_{dw} as a free parameter.

As there are only four long-term NR simulations from Rosswog et al. (2014), the simulation set is not large enough for our interpolator to gain meaningful constraints (MacKay 1998). However, since the general shape of each NR simulation geometry was seen to be toroidal (see Fig. 2) in Rosswog et al. (2014), we fit a Gaussian-toroid described by three free parameters: In cylindrical coordinates, it is defined as

$$\rho_{dyn}(v_r, v_z) = \begin{cases} \rho_0 \exp\left(\frac{-(v_r - v_{tor})^2 + (v_z/a)^2}{2\sigma^2}\right) & f(v_r, v_z) \leq v_{dyn} \\ 0 & f(v_r, v_z) > v_{dyn} \end{cases}, \tag{5}$$

where $f(v_r, v_z) = \sqrt{(v_r - v_{tor})^2 + (v_z/a)^2}$. Here, ρ_0 is a density coefficient proportional to the ejecta mass, $v_r = \sqrt{v_x^2 + v_y^2}$ is the radial velocity, $v_{tor} = 0.059\,c + v_{dyn}$ represents the central velocity of the toroid (with $0.059c$ as the fixed inner velocity), a is the axial ratio, and $\sigma = v_{dyn}/3.5$ is the standard deviation of the Gaussian.

To minimize the number of dimensions for the Gaussian Process interpolator − we discuss why we minimize the dimension and the Gaussian Process interpolator in more detail in Section 3.1− we fixed v_{tor} and σ to those values that minimized the χ^2 value. We then simulated a grid of dynamical and disc–wind geometries as in Table 2, and added the light curves together post-simulation as done for the ElDC model. We present the χ^2-minimization fits in Fig. 2. Notice that the functional fit that we chose in equation (5) seems to match the form of the NR simulations from Rosswog et al. (2014) quite well. Furthermore, the bottom panels are very similar to the middle panels, with perhaps slightly extended boundaries, and the reduced χ^2s are only slightly larger. We also found no noticeable discrepancy between the light curves produced by these geometries, further indicating that these approximations are appropriate approximating the light curves of these NR simulated ejecta. We emphasize that our parametrization by the five parameters in Table 2 therefore *contains* the models A–D of Rosswog et al. (2014).

As with the ElDC and ElDCr simulation sets, we constructed both a simulation set where the ejecta were processed independently, and a simulation set with 'reprocessing.' The dynamical grid had

Table 2. Summary of the parameters in the TorS geometry simulated in POSSIS.

Ejecta type	Parameter	Parameter values
Dynamical	$M_{ej, 1}$	[0.001, 0.01, 0.025, 0.04, 0.055, 0.07, 0.085, 0.1] $M_\odot$
Dynamical	a	[0.25, 0.5, 0.75, 1, 1.5, 2]
Dynamical	v_{dyn}	[0.04, 0.085, 0.12, 0.155, 0.2, 0.25]c
Disc wind	$M_{ej, 2}$	[0.001, 0.01, 0.025, 0.04, 0.055, 0.07, 0.085, 0.1] $M_\odot$
Disc wind	v_{dw}	[0.1, 0.15, 0.2, 0.25, 0.3, 0.35]c

Notes. $M_{ej, 1}$ refers to the total mass in the lanthanide-rich region, v_{dyn} parameterizes the geometric scale of the toroidal lanthanide-rich region, and a represents the axial ratio between the height and width of the cross-sectional ellipse. $M_{ej, 2}$ refers to the total mass in the lanthanide-free region, and v_{dw} refers to the maximum velocity of the spherical lanthanide-free disc wind region. See the right-hand panel of Fig. 1 for a depiction of v_{dyn}, a, and v_{dw} in the TorS model.

$8 \times 6 \times 6 = 288$ simulations, and the disc wind grid had $8 \times 6 = 48$ simulations. As we will mention in Section 3, we reduced the simulation set for 'reprocessing', as a full grid would require $288 \times 48 = 13\,824$ simulations, which is more than we can feasibly do. In addition, training the Gaussian Process Interpolator is the bottleneck for our analysis procedure, not producing simulations. Thus, rather than produce a full simulation set, we reduced the number of parameters in each dimension by a factor of 2, so in the end we only created 432 simulations.

We refer to this simulation set and the derived model as the TorS model. With reprocessing accounted for, we call it the TorS reprocessing (TorSr) model.

3 INCLINATION AND INTERPRETATION OF GW170817

Now that we have simulated the light curves for the five different models, SSCr, ElDC, ElDCr, TorS, and TorSr, we will use these to constrain the model parameters for GW170817/AT2017gfo. First, since we want our constraints to be over a continuous range, and our simulations were only over a discrete parameter grid, we use a Gaussian Process Regression method to interpolate the simulated light curves. Gaussian Process Regression has numerous advantages, and it is particularly useful for inference because it is Bayesian in nature. Many machine learning algorithms would be able to interpolate the light curves over the continuous parameter space, however Gaussian Process is special in its ability to also estimate the uncertainties associated with the predicted light curves.

When the Gaussian Process Regression algorithm is trained over our complete parameter grid, it can estimate the light curves produced from any arbitrary parameter combination, but large uncertainties make the estimation meaningless if the input parameter vector lies well outside the training grid. We call this phenomenological function a *surrogate* model, and we build a surrogate model for each of our simulation grids (SSCr, ElDC, ElDCr, TorS, and TorSr). We then use each of these surrogate models to do Bayesian inference on AT2017gfo.

3.1 Inclination-dependent surrogates

To use these simulations in the surrogate light-curve models, we introduce a modification to our previous technique (Coughlin et al. 2017; Coughlin et al. 2018; Coughlin et al. 2019). We use the five

Table 3. A summary of the priors used for the inference in each surrogate model.

| Model	Parameter	Prior lower bound	Upper bound
SSCr	$\log_{10}(M_{ej}/M_\odot)$	-3	0
	Φ	$0°$	$90°$
	θ_{obs}	$0°$	$90°$
ElDC(r)	$\log_{10}(M_{ej, 1}/M_\odot)$	-3	0
	$\log_{10}(M_{ej, 2}/M_\odot)$	-3	0
	a	1	10
	q_0	$0°$	$90°$
	θ_{obs}	$0°$	$90°$
TorS(r)	$\log_{10}(M_{ej, 1}/M_\odot)$	-3	0
	$\log_{10}(M_{ej, 2}/M_\odot)$	-3	0
	a	0.25	2
	v_{dyn}	0.04c	0.25c
	v_{dw}	0.1c	0.35c
	θ_{obs}	$0°$	$90°$

Notes. The priors were kept the same for both the non-reprocessing and reprocessing cases, i.e. TorS(r) means the TorS and TorSr models. All priors are taken to be uniform between the lower and upper bound.

different grids of radiative transfer simulations described above as training for a Gaussian Process Regression based method. This allows us to interpolate the light curves across the continuous parameter space of interest. To do so, we take each simulation and compute u-, g-, r-, i-, z-, y-, J-, H-, and K-band light curves as a function of the viewing angle. Not only is the Gaussian process non-parametric, so the form of our parametrization for each model will not introduce bias into the parameter estimation, but it also is Bayesian in nature; by comparing the inferred light curve for a set of parameters to the measured light curve for AT2017gfo, we can compute likelihoods based on a given set of model parameters. For each of the simulation sets, we assume flat priors (flat in log for the ejecta masses) that span the full parameter space we simulated, but usually do not extend far beyond the simulations. We show the lower and upper bounds for each parameter in each surrogate model in Table 3, and the priors were the same for the reprocessing versus the separately simulated KNe.

For the reprocessing simulation sets, the full set of simulated training data was too large for the Gaussian Process computation to sample effectively, so we instead trained the algorithm on a stratified set, decimated by a factor of 2 in each dimension (except for the inclination angle). We determined that the reduced training set provided appropriate constraints by comparing constraints from the stratified sample to those with a smaller sample; these were shown to be indistinguishable, and therefore we expect that adding more training light curves would not have led to a noticeable improvement.

3.2 Parameter estimation

With the surrogates in hand, we calculate the likelihood as a function of the geometry parameters. In general, we have the ability to allow for a time shift and distance, but we fix these to match the known values for AT2017gfo. Over this n-dimensional parameter space (four dimensional for the SSCr model, six for ElDC and ElDCr, and seven for TorS and TorSr; the number of geometry parameters plus two parameters for inclination and physical distance − which affects the light-curve AB magnitudes), we then obtain posteriors for the most likely geometry for each model, and the corresponding light curve predicted by the model. In Fig. 3, we show the maximum-likelihood χ^2 fit to the light-curve data of GW170817, drawn from Coughlin et al. (2019), using each of the five models, while in Fig. 4, we
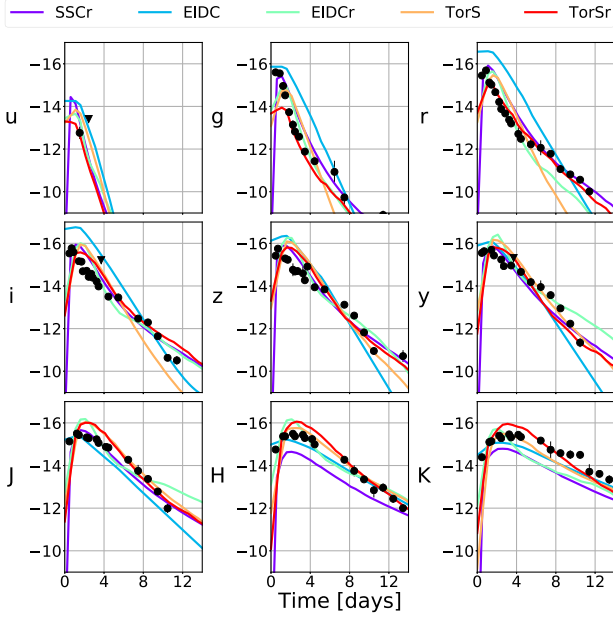
Figure 3. Light curves for the inclination-dependent surrogate KN models with the points of GW170817 included (with the data taken from the sample from Coughlin et al. 2019). The light curves shown correspond to a maximum likelihood χ^2 fit to the data for the intrinsic parameters, assuming a ± 0.5-mag uncertainty in the light-curve fitting, in quadrature with the photometric uncertainty from the data. All the light curves are expressed in AB absolute magnitudes. The circles denote actual detections while the triangles are upper limits. The letters to the left of the *y*-axes show the passbands of the observations. Purple is the SSCr model with a reduced χ^2 of 2.80, light blue is the ElDC model with a reduced χ^2 of 4.18, light green is the ElDCr model with a reduced χ^2 of 1.85, orange is the TorS model with a reduced χ^2 of 3.70, and in red is the TorSr model with a reduced χ^2 of 1.79.
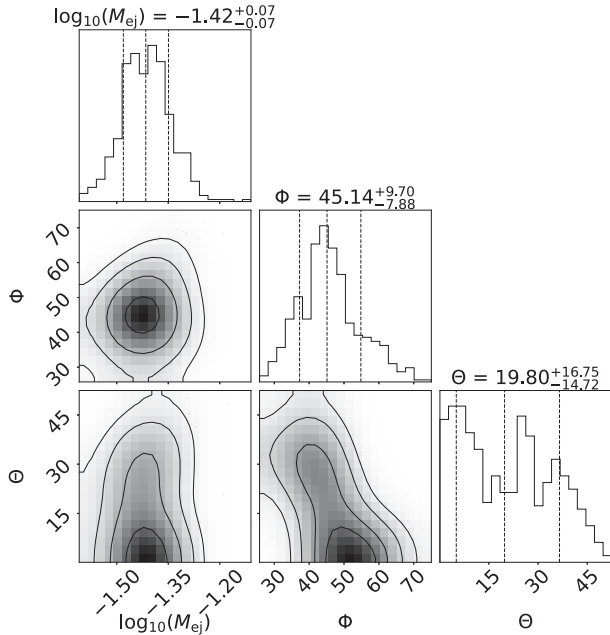
Figure 4. Corner plot showing posteriors of GW170817 for the SSCr model assuming an uncertainty of ± 0.5 mag added in quadrature with the measurement uncertainty for the light-curve fitting.

show an example corner plot for the posteriors on the simulation parameters in the SSCr simulation set.

We are interested in comparing the constraints for model parameters represented by the different ejecta geometries. As a metric for the 'agreement' or 'overlap' between the posteriors $f_1, ..., f_n$, we will use the *Matusita affinity* (Matusita 1967; Toussaint 1974),

$$A = \int [f_1(x)...f_n(x)]^{1/n} \, \mathrm{d}x. \tag{6}$$

In this formalism, if all the posterior density functions are identical, then $A = 1$, and if any two are absolutely disjoint, then $A = 0$. The integrand is the geometric mean of the posterior densities, and in general, has the property of being higher if the n posterior densities are closer in value. This functional is close to 1 if the n posteriors are similar in form, and close to 0 if they are different (see Matusita 1967; Toussaint 1974, for more details and properties).

The Matusita affinity is sensitive to the form of each posterior distribution function. That is, it not only quantifies consistency in posteriors, but also in form. For example, a constraint of $-2.1 \leq \log_{10}(M_{ej}) \leq 0.1$ is consistent with a constraint of $-1.3 \leq \log_{10}(M_{ej}) \leq -1.1$, but there is some notion of an inconsistency in *form*. For our purposes, we want to be able to quantify both these notions of consistency, so this Matusita affinity is appropriate.

We show the posteriors for the inclination angle, total ejecta mass, and ejecta mass ratio in Fig. 5. On the left-hand column of Fig. 5, we show the posteriors for the fits when we set the systematic error to ± 0.5 mag, added in quadrature with the measured photometric uncertainty in the samples of AT2017gfo, collected from the data set described in Coughlin et al. (2019). We summarize the posteriors in Table 4. The first interesting result that we see is that fits with reprocessing included result in posteriors with narrower distributions. To understand this, consider the example of the TorSr model versus TorS model case. Light curves produced by the TorSr model will likely have a stronger inclination dependence; to first order the TorSr and TorS light curves should match, but for the TorSr, there is a second-order term for the inclination dependent *suppression* of the 'red' ejecta by the 'blue' ejecta and vice versa. Given any covariance between the posteriors for other parameters and the inclination angle, a sharper peak in inclination angle constraints could cause a sharper peak in the posteriors for other parameters, in the absence of any other effects changing the sharpness of the posterior peak.

Secondly, notice that in each of the posteriors, the ElDCr seems to be in disagreement with the other posteriors. We will quantify this disagreement by using Equation 6. For the inclinations, $A_{inc} = 0.01$. However, motivated by the qualitative disagreement from the ElDCr posterior from each of the others, we want to see how the affinity changes if we remove the ElDCr posterior, and consider the affinity from the other four models. However, it is not clear how the Matusita affinity functional changes when the number of posteriors (n in equation 6) changes from 5 to 4. Therefore, we will *replace* the ElDCr posterior with what we used as a prior (simply uniform across $0 \leq \theta_{obs} \leq 90$, see Table 3), then the affinity increases significantly, to $A'_{inc} = 0.27$ (the prime denotes that we are using a prior instead of a posterior). Because of the surprisingly narrow posterior for this constraint, we examined the inferred light curves for the ElDCr models directly. For $\theta_{obs} \notin [0°, 3°]$, the light curves diverge from AT2017gfo, particularly for late times in the NIR bands. This is consistent with the posterior shown in Fig. 5.

For the ejecta masses, $A_{mass} = 0.004$. This time, however, *both* the ElDCr and the ElDC model are very different qualitatively. They both infer very large ejecta masses, inconsistent with inference from
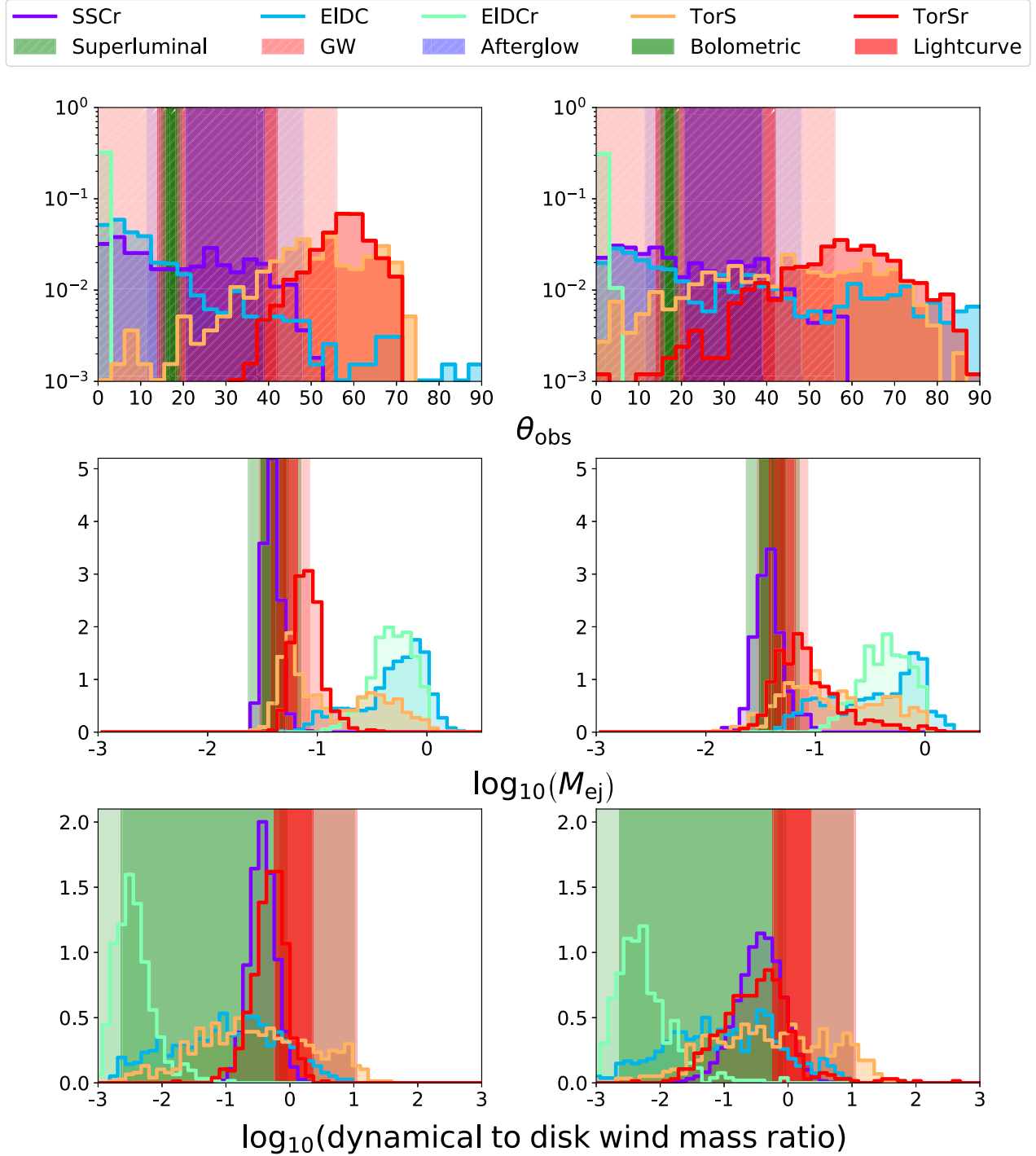
Figure 5. Histograms for the inclination angle (top row), ejecta masses (middle row), and dynamical to disc wind mass ratio (bottom row) constraints based on the five different surrogate models, assuming a ±0.5 (left-hand panel) and ±1.0 mag (right-hand panel) uncertainty for the light-curve fitting. Dark blue is the SSCr model, light blue is the ElDC model, light green is the ElDCr model, orange is the TorS model, and in red is the TorSr model. In the top row, we also include constraints from GWs (Abbott et al. 2017), afterglow modelling (Troja et al. 2019), and superluminal motion Hotokezaka et al. (2019). In the middle and bottom rows, we also include the constraints derived from Coughlin et al. (2018), which uses our previous method.

the other models. When we suppress the ElDC and ElDCr posteriors and replace them with the uniform priors, $A'_{mass} = 0.22$.

We can also derive constraints for the dynamical to disc wind mass ratio. Like in the inclination angle case, all the models appear to constrain the dynamical to disc wind mass ratios broadly similarly,

except for the ElDCr model. Quantitatively, when we compare the five posteriors, we find the Matusita affinity for the posteriors is $A_{ratio} = 0.10$, and without the ElDCr model, $A'_{ratio} = 0.53$.

This indicates that the ElDC and ElDCr models yield fundamentally different results from the SSCr and the TorS and TorSr models.

Table 4. A summary of the posteriors inferred in each surrogate model, for the inclination angle $\theta_{\rm obs}$, the log-ejecta mass $\log_{10}(M_{\rm ej}/{\rm M_\odot})$ in terms of solar masses, and the logarithm of the dynamical to disc wind mass ratio $\log_{10}({\rm ratio})$.

Parameter	Model	0.5-mag uncertainty	1.0-mag uncertainty
$\theta_{\rm obs}$	SSCr	20^{+17}_{-15}	19^{+20}_{-13}
	ElDC	10^{+22}_{-7}	29^{+38}_{-23}
	ElDCr	$1.2^{+0.4}_{-0.5}$	$1.6^{+0.6}_{-0.7}$
	TorS	52^{+14}_{-13}	44^{+16}_{-25}
	TorSr	58^{+5}_{-7}	58^{+13}_{-15}
$\log_{10}(M_{\rm ej}/{\rm M_\odot})$	SSCr	$-1.4^{+0.1}_{-0.1}$	$-1.4^{+0.1}_{-0.1}$
	ElDC	$-0.3^{+0.2}_{-0.6}$	$-0.5^{+0.4}_{-0.6}$
	ElDCr	$-0.3^{+0.2}_{-0.2}$	$-0.4^{+0.2}_{-0.3}$
	TorS	$-0.9^{+0.6}_{-0.4}$	$-0.8^{+0.6}_{-0.4}$
	TorSr	$-1.1^{+0.1}_{-0.1}$	$-1.1^{+0.6}_{-0.2}$
$\log_{10}({\rm ratio})$	SSCr	$-0.4^{+0.2}_{-0.2}$	$-0.5^{+0.3}_{-0.4}$
	ElDC	$-1.0^{+0.8}_{-1.0}$	$-1.0^{+0.8}_{-0.9}$
	ElDCr	$-2.4^{+0.4}_{-0.2}$	$-2.3^{+0.7}_{-0.3}$
	TorS	$-0.5^{+1.0}_{-0.9}$	$-0.3^{+1.0}_{-0.9}$
	TorSr	$-0.3^{+0.2}_{-0.3}$	$-0.5^{+0.4}_{-0.6}$

Notes. In the third column are the posteriors when the systematic error budget is set to ±0.5 mag, and the fourth column is with a systematic error budget of ±1.0 mag. The mean of the posterior is given, as well as the upper and lower 68 per cent credible intervals. All angles are measured in degrees.

Given the inconsistency with the other models *and* other forms of inclination, ejecta mass and mass ratio measurements (Abbott et al. 2017; Coughlin et al. 2018; Hotokezaka et al. 2019; Troja et al. 2019), the ElDC model is disfavoured as being a geometry that encapsulates AT2017gfo particularly well.

We can also use this method to probe the level of systematic errors within the models. To determine the effect of the assumed systematic error on the posteriors, we show posteriors when ±1.0 mag is added in quadrature to the measurement error on the right-hand column of Fig. 5. As expected, the Matusita affinities indicate much more consistent posteriors, with the cost of less constraining posteriors. For the inclinations, $A_{\rm inc} = 0.09$, and ignoring the ElDCr model, $A'_{\rm inc} = 0.67$. This is also the case when considering the ejecta masses: $A_{\rm mass} = 0.06$, and ignoring the ElDC and ElDCr models, $A'_{\rm mass} = 0.37$. For the ejecta mass ratio between the dynamical ejecta and the disc wind ejecta, the affinity again increases significantly when a larger uncertainty is used for the fitting: $A_{\rm ratio} = 0.41$, and without the ElDCr model, $A'_{\rm ratio} = 0.71$. Notice that the affinities increase substantially with a ±1.0-mag error budget. This indicates that the ±1.0-mag systematic error budget is generally more appropriate, when more specific information about the geometry of the KN is unknown.

4 CONCLUSION

In this paper, we have used a combination of KN model grids for a variety of ejecta geometries in combination with Gaussian Process Regression to infer source parameters from the AT2017gfo light curve. Using this method on different geometries and comparing the inferred constraints, we find that the inferred constraints tend to be sensitive to the underlying geometry. In particular, we have found

that taking into account reprocessing effects gives a much better fit to AT2017gfo; this method has also shown that the resulting inclination constraint from the inclusion of reprocessing can yield constraints inconsistent with those measured by other methods. Indeed, the large disagreement between the ElDCr model's constraint on the inclination angle and the measurements by analyses such as Abbott et al. (2017), Troja et al. (2019), Hotokezaka et al. (2019), and Finstad et al. (2018) implies that this geometry may not be appropriate to describe AT2017gfo. Our method can therefore be used to constrain the form of the geometry of the KNe – when radiative reprocessing is accounted for, the geometry of the KN associated with AT2017gfo could not have been of the form of the ElDC geometry.

It is likely the case that the ejecta geometry is dependent on the progenitor initial conditions; the ElDC geometry could likely be more consistent with a future KN observation. Our method, over many detections, will be able to measure how the geometry depends on the progenitor.

We also showed that the Matusita affinity increases dramatically for the inclination angle constraints (and increases a bit more modestly for the ejecta mass and ratio constraints) when an uncertainty of ±1 mag is used in quadrature with the measurement uncertainty, as opposed to the nominal 0.5 mag. For this reason, we recommend using at least an uncertainty of ±1 mag in light-curve fitting for inclination angle constraints until systematic uncertainties are better under control.

Our method has also shown how to evaluate the efficacy of certain geometries or constrain the geometry of KN ejecta, i.e. it is not necessarily bad that differently constructed but reasonable geometries seem to disagree with one another. In a future work, using a larger range of possible geometries, one could investigate the possibility of more directly constraining the geometry of KN ejecta using a modification of our technique here.

Altogether, this analysis shows that using more sophisticated and realistic geometry sets, parameterized according to physical variables, should be encouraged. These could be constructed using long-term numerical-relativity simulations directly, for example, as opposed to the more common subjective geometrical parameters. In the short term, however, analyses going forward should use more agnostic geometries, i.e. those one that strike the right balance between approximating a KN geometry and being non-committal to any specific features, such as those achieved in the SSCr geometry.

DATA AVAILABILITY

The data underlying this paper are derived from public code found here:

https://github.com/mcoughlin/gwemlightcurves.

The POSSIS simulations are available at:

https://github.com/mbulla/kilonova_models.

REFERENCES

Abbott B. P. et al., 2017, Phys. Rev. Lett., 119, 161101

Abbott B. P. et al., 2017, Nature, 551, 85

Agathos M., Zappa F., Bernuzzi S., Perego A., Breschi M., Radice D., 2020, Phys. Rev. D, 101, 044006

Alexander K. D. et al., 2017, ApJ, 848, L21

Annala E., Gorda T., Kurkela A., Vuorinen A., 2018, Phys. Rev. Lett., 120, 172703

Arcavi I., 2018, ApJ, 855, L23

Barnes J., Kasen D., Wu M.-R., Martínez-Pinedo G., 2016, ApJ, 829, 110

Bauswein A., Baumgarte T. W., Janka H.-T., 2013, Phys. Rev. Lett., 111, 131101

Bauswein A., Just O., Janka H.-T., Stergioulas N., 2017, ApJ, 850, L34

Bauswein A., Blacker S., Lioutas G., Soultanis T., Vijayan V., Stergioulas N., 2020, arXiv:2010.04461

Bulla M., 2019, MNRAS, 489, 5037

Bulla M., Sim S. A., Kromer M., 2015, MNRAS, 450, 967

Burns C. R. et al., 2018, ApJ, 869, 56

Capano C. D. et al., 2020, Nat. Astron., 4, 625

Carracedo A. S., Bulla M., Feindt U., Goobar A., 2020, arXiv:2004.06137

Chen H.-Y., 2020, Phys. Rev. Lett., 125, 201301

Chornock R. et al., 2017, ApJ, 848, L19

Coughlin M., Dietrich T., Kawaguchi K., Smartt S., Stubbs C., Ujevic M., 2017, ApJ, 849, 12

Coughlin M. W. et al., 2018, MNRAS, 480, 3871

Coughlin M. W., Dietrich T., Margalit B., Metzger B. D., 2019, MNRAS, 489, L91

Coughlin M. W. et al., 2020a, Phys. Rev. Res., 2, 022006

Coughlin M. W. et al., 2020b, Nat. Commun., 11, 4129

Cowperthwaite P. S . et al., 2017, ApJ, 848, L17

Dessart L., Ott C., Burrows A., Rosswog S., Livne E., 2009, ApJ, 690, 1681

Dhawan S., Bulla M., Goobar A., Carracedo A. S., Setzer C., 2020, ApJ., 888, 67

Dietrich T., Ujevic M., 2017, Class. Quantum Gravity, 34, 105014

Dietrich T., Coughlin M. W., Pang P. T. H., Bulla M., Heinzel J., Issa L., Tews I., Antier S., 2020, Science, 370, 1450

Drout M. R. et al., 2017, Science, 358, 1570

Evans P. A. et al., 2017, Science, 358, 1565

Fernández R., Kasen D., Metzger B. D., Quataert E., 2015, MNRAS, 446, 750

Finstad D., De S., Brown D. A., Berger E., Biwer C. M., 2018, ApJ, 860, L2

Foucart F., 2012, Phys. Rev. D, 86, 124007

Foucart F., O'Connor E., Roberts L., Kidder L. E., Pfeiffer H. P., Scheel M. A., 2016, Phys. Rev. D, 94, 123016

Foucart F., Hinderer T., Nissanke S., 2018, Phys. Rev. D, 98, 081501

Haggard D., Nynka M., Ruan J. J., Kalogera V., Cenko S. B., Evans P., Kennea J. A., 2017, ApJ, 848, L25

Hallinan G. et al., 2017, Science, 358, 1579

Hotokezaka K., Kiuchi K., Kyutoku K., Okawa H., Sekiguchi Y.-i., Shibata M., Taniguchi K., 2013, Phys. Rev. D, 87, 024001

Hotokezaka K., Nakar E., Gottlieb O., Nissanke S., Masuda K., Hallinan G., Mooley K. P., Deller A. T., 2019, Nat. Astron., 3, 940

Kasen D., Thomas R. C., Nugent P., 2006, ApJ, 651, 366

Kasen D., Fernandez R., Metzger B., 2015, MNRAS, 450, 1777

Kasen D., Metzger B., Barnes J., Quataert E., Ramirez-Ruiz E., 2017, Nature, 551, 80 EP

Kasliwal M. M. et al., 2017, Science, 358, 1559

Kawaguchi K., Kyutoku K., Shibata M., Tanaka M., 2016a, ApJ, 825, 52

Kawaguchi K., Kyutoku K., Shibata M., Tanaka M., 2016b, ApJ, 825, 52

Kawaguchi K., Shibata M., Tanaka M., 2018, ApJ, 865, L21

Kawaguchi K., Shibata M., Tanaka M., 2020, ApJ, 889, 171

Kilpatrick C. D. et al., 2017, Science, 358, 1583

Kiuchi K., Sekiguchi Y., Kyutoku K., Shibata M., Taniguchi K., Wada T., 2015, Phys. Rev. D, 92, 064034

Kóbori J., Bagoly Z., Balázs L. G., 2020, MNRAS, 494, 4343

Köppel S., Bovard L., Rezzolla L., 2019, ApJ, 872, L16

Korobkin O., Rosswog S., Arcones A., Winteler C., 2012, MNRAS, 426, 1940

Korobkin O. et al., 2020, preprint(arXiv:2004.00102)

Krüger C. J., Foucart F., 2020, Phys. Rev. D, 101, 103002

Lattimer J. M., Schramm D. N., 1974, ApJ, 192, L145

Li L.-X., Paczynski B., 1998, ApJ, 507, L59

McCully C. et al., 2017, ApJ, 848, L32

MacKay D., 1998, in Bishop C. M.ed. NATO ASI Series, NeuralNetworks and Machine Learning, Kluwer Academic Press, p. 133

Margutti R. et al., 2017, ApJ, 848, L20

Martin D., Perego A., Arcones A., Thielemann F.-K., Korobkin O., Rosswog S., 2015, ApJ, 813, 2

Matusita K., 1967, Ann. Inst. Stat. Math., 19, 181

Metzger B. D., 2020, Living Rev. Relativ., 23, 1

Metzger B. D. et al., 2010, MNRAS, 406, 2650

Most E. R., Weih L. R., Rezzolla L., Schaffner-Bielich J., 2018, Phys. Rev. Lett., 120, 261103

Nicholl M. et al., 2017, ApJ, 848, L18

Pannarale F., Tonita A., Rezzolla L., 2011, ApJ, 727, 95

Perego A., Rosswog S., Cabezón R. M., Korobkin O., Käppeli R., Arcones A., Liebendörfer M., 2014, MNRAS, 443, 3134

Perego A., Radice D., Bernuzzi S., 2017, ApJ, 850, L37

Pian E. et al., 2017, Nature, 551, 67

Radice D., Dai L., 2019, Eur. Phys. J., A55, 50

Radice D., Perego A., Zappa F., Bernuzzi S., 2018a, ApJ, 852, L29

Radice D., Perego A., Hotokezaka K., Fromm S. A., Bernuzzi S., Roberts L. F., 2018b, ApJ, 869, 130

Roberts L. F., Kasen D., Lee W. H., Ramirez-Ruiz E., 2011, ApJ, 736, L21

Rosswog S., Korobkin O., Arcones A., Thielemann F.-K., Piran T., 2014, MNRAS, 439, 744

Shappee B. J. et al., 2017, Science, 358, 1574

Siegel D. M., Metzger B. D., 2017, Phys. Rev. Lett., 119, 231102

Smartt S. J. et al., 2017, Nature, 551, 75 EP

Tanaka M., Hotokezaka K., 2013, ApJ, 775, 113

Tanaka M., Hotokezaka K., 2013, ApJ, 775, 113

Tanaka M. et al., 2018, ApJ, 852, 109

Toussaint G., 1974, Ann. Inst. Stat. Math., 26, 389

Troja E. et al., 2017, Nature, 551, 71

Troja E. et al., 2019, MNRAS, 489, 1919

Utsumi Y. et al., 2017, PASJ, 69, 101

Villar V. A. et al., 2017, ApJ, 851, L21

Wanajo S., Sekiguchi Y., Nishimura N., Kiuchi K., Kyutoku K., Shibata M., 2014, ApJ, 789, L39

Wollaeger R. T. et al., 2018, MNRAS, 478, 3298